Solid State Ionics 421 (2025) 116804

Contents lists available at ScienceDirect

Solid State Ionics

journal homepage: www.elsevier.com/locate/ssi

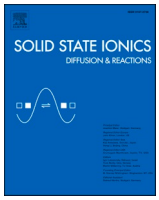

Structural analysis of the $LiCoO_2$ cathodes/garnet-type $Li_{6.5}La_3Zr_{1.5}Ta_{0.5}O_{12}$ solid electrolyte interface

K. Niitsu [a,*], F. Ichihara [b], S. Miyoshi [b], M. Ode [c], K. Mitsuishi [a], T. Masuda [b,d], K. Takada [b]

[a] Center for Basic Research on Materials, National Institute for Materials Science (NIMS), Tsukuba, Ibaraki 305-0047, Japan
[b] Research Center for Energy and Environmental Materials (GREEN), National Institute for Materials Science (NIMS), Tsukuba, Ibaraki 305-0044, Japan
[c] Research Center for Structural Materials, National Institute for Materials Science (NIMS), Tsukuba, Ibaraki 305-0047, Japan
[d] Graduate School of Chemical Sciences and Engineering, Hokkaido University, Sapporo, Hokkaido 060-0810, Japan

ARTICLE INFO

Keywords:
Lithium cobalt oxide
Solid-state reaction
Interfacial reaction
Densification
Scanning transmission electron microscopy

ABSTRACT

The sinterability of oxide cathode $LiCoO_2$ and garnet-type solid electrolyte $Li_{7-x}La_3Zr_{2-x}Ta_xO_{12}$ ($x = 0.5$) at 980 and 1080 °C has been studied using an integrated suite of scanning transmission electron microscopy and spectroscopic techniques, with a particular focus on the $LiCoO_2/Li_{7-x}La_3Zr_{2-x}Ta_xO_{12}$ interfaces. Whereas the densification hardly progresses and the interdiffusion is limited to the vicinity of the interface at 980 °C, dramatic densification can be achieved at 1080 °C at the expense of severe interfacial modification. The structural, chemical, and electronic characteristics of the interphases are systematically investigated. Two kinds of interphases are formed: one has a disordered $LiCoO_2$ structure, thickly forming in contact with $LiCoO_2$, and the other has a structural and chemical character similar to $Li_{7-x}La_3Zr_{2-x}Ta_xO_{12}$, thinly forming in contact with $Li_{7-x}La_3Zr_{2-x}Ta_xO_{12}$. The former is assumed to play a vital role in the densification of the pellet. Analysis using energy-dispersive spectroscopy and electron energy loss spectroscopy reveals that the disordered $LiCoO_2$ interphase is somewhat depleted of Li and contaminated with La, Zr, and Ta. These properties are considered less favorable for achieving undisturbed ionic conductivity.

1. Introduction

Bulk-type all-solid-state lithium-ion batteries (ASSLIBs) are placed as the promising candidate of the next generation of rechargeable batteries in view of the safe and stable operation with high energy and power densities [1]. In addition to the search for potential solid electrolytes and electrode materials, their interfacial reaction is of particular interest because the interfacial resistance can be a major bottleneck for the development of ASSLIBs. Since the interfaces owe various aspects of the performance such as quality stability, thermal stability, cycling durability, besides power density, well-defined and well-tailored interfaces with high ionic conductivity are essential for practical use [2]. Nevertheless, interfacial reactions in lithium-ion conductive materials are generally less tractable: the type of interfacial products depends on various thermodynamic factors such as temperature, chemical potential, and pressure, and even local/non-thermodynamic factors such as morphology, crystallographic orientation, contamination, and time.

Among various Li-ion conductive materials, garnet-type oxide $Li_7La_3Zr_2O_{12}$ (LLZ) is expected to be one of the promising solid electrolytes as this compound conveys relatively high conductivity (~5 $\times$ 10^{-4} S/cm at ambient temperature) in bulk with high chemical stability, good compatibility with Li metal and wide potential window [3–6]. This high conductivity has been recorded for the cubic symmetry but is reduced by about two orders of magnitude for tetragonal symmetry [7,8]. Recent studies have elucidated that Ta substitution helps stabilize the cubic structure and enhance the ionic conductivity (~ 10^{-3} S/cm) [8,9]. The chemical formula $Li_{7-x}La_3Zr_{2-x}Ta_xO_{12}$ (LLZT) with $x =$ 0.5–0.6 has been found to be optimal [8–10]. As a counterpart cathode material, a layered rock-salt-type $LiCoO_2$ (LCO) is the de facto standard [11,12]. As well as its lamellar structure allows for the reversible intercalation of Li ions, its high compacted density, high energy density, and prominent cycle durability and reliability are also outstanding advantages for its use as a cathode material for ASSLIBs.

The LLZ/LCO interfacial characters have been studied elsewhere. Kim has reported that the La_2CoO_4 with a thickness of ~50 nm is formed at the LCO/LLZ interface deposited at 700 °C in air and makes the electrochemical performance poor [3]. Kato has elucidated that inserting a thin Nb metal layer between the LCO and LLZ at 600 °C results in

* Corresponding author.
E-mail address: NIITSU.Kodai@nims.go.jp (K. Niitsu).

https://doi.org/10.1016/j.ssi.2025.116804
Received 10 December 2024; Received in revised form 28 January 2025; Accepted 1 February 2025
Available online 10 February 2025

the formation of a Li-ion-conductive amorphous layer [13]. These studies have addressed the modifications of the LCO/LLZ interface at relatively low temperatures where the sintering reaction does not apparently proceed. Compared to sulfide solid electrolytes, oxide solid electrolytes are generally brittle and require higher temperatures to densify the electrolyte/electrode mixture. As the sintering temperature increases, it is anticipated that interfacial mutual diffusion is pronounced and thus makes the chemical bonding strong, but instead such modification comes at the expense of interfacial ionic conductivity. Toward the implementation of oxide solid electrolytes for ASSLIBs, achieving densification while obtaining an interface with good ionic conductivity is a significant challenge. Although being envisaged as challenging, high-temperature sintering will straightforwardly commit to the densification of the mixture. The interfacial reactions at high temperatures could be informative in getting the strategy for engineering desirable interfaces and microstructures for various combinations of derivative/family materials [14].

In this study, the mixture of LLZT and LCO powders is sintered at high temperatures, and resultant microstructures are studied using an integrated suite of scanning transmission electron microscope (STEM), energy dispersive X-ray spectroscopy (EDS), and electron energy loss spectroscopy (EELS). In response to the difference in sintering temperature, dramatic changes in the microstructures and interfacial characters are observed. These changes are also manifested as latent heat detected by thermal analysis. Detailed investigations on the morphology, chemistry, atomistic structure, and valence state are systematically performed for the interfacial products. This will help to shed light on the out-of-equilibrium complex interfacial reactions, which provides the prospects and challenges toward realizing the high-temperature fabrication of ASSLIBs.

2. Experimentals and calculations

LLZT ($Li_{7-x}La_3Zr_{2-x}Ta_xO_{12}$; $x = 0.5$) and LCO powders from Toshima Manufacturing Co. Ltd. were used. The median diameters of the pristine LLZT and LCO powders are 6 μm and 1 μm, respectively, and the analyzed compositions precisely agree with the nominal ones. The LCO and LLZT powders were mixed in a 1:1 volume ratio (9:1 M ratio) without adding excess lithium source. The mixture was sintered at 980 and 1080 °C for 10 h under O_2 flow, followed by furnace cooling. The sintered pellets were polished, and the inner facets were subjected to X-ray diffraction (XRD) measurements. Thermogravimetric-differential thermal analysis (TG-DTA) was performed on the unsintered mixture with a heating rate of 2 °C/min in the range of 20–1000 °C and 0.5 °C/min in the range of 1000–1100 °C under 95 %O_2–5 %Ar gas flow. The fracture surfaces of the sintered pellets were observed using a scanning electron microscope (SEM: JCM-7000, JEOL Ltd.). A thin-foiled specimen with a dimension of 10 μm × 5 μm × 0.1 μm for the TEM observation was lifted from the inner side of the sintered pellets using a focused ion beam (JIB-4501, JEOL Ltd.) equipped with a cooling stage. The processing temperature was set to −173 °C. The microstructural observation was carried out using a 200-kV STEM (JEM-ARM200F, JEOL Ltd.). EDS and EELS mappings were obtained by their detectors installed onto the STEM.

The thermodynamic calculations were carried out using the commercial package FactSage 8.3, developed by GTT-Technologies, together with the thermodynamic data from the ab initio Materials Project (aiMP). This approach was employed to gain insight into the phase stability and possible interfacial products. The calculation system is LCO/LLZT mixture in a 9:1 M ratio under partial oxygen pressure $P_{O2} = 0.21$ atm. Note that the Gibbs free energy of LLZT was simply approximated as a linear combination of those of $Li_7La_3Zr_2O_{12}$ (space group: $I4_1/acd$) and $Li_5La_3Ta_2O_{12}$ (space group: $Ia\bar{3}d$).

3. Results

3.1. XRD, TG-DTA and thermodynamic calculations

The DTA curve in Fig. 1 indicates that the sintering reaction gets active above 1000 °C. The associated weight loss in the corresponding TG curve is expected to be due to the sublimation of lithium oxides. Although sensitively dependent on experimental conditions such as atmosphere, pressure, purity of raw materials, particle size and shape, and mixture density, the thermal behavior in Fig. 1 seems reasonable in light of the respective thermal behaviors of LCO and LLZ reported elsewhere: Antolini and Ferretti reported that the decomposition of LCO takes place in air above 900 °C [15], and Zhang and Yang respectively reported that the sintering reaction of doped LLZ proceeds above 980 °C [16,17].

SEM images of the fracture surfaces of pellets sintered at 980 and 1080 °C are shown in Fig. 2(a) and (b), respectively. While the microstructure sintered at 980 °C does not show significant morphological changes, sintering at 1080 °C promotes the microstructural coarsening and forms well-contacting LCO/LLZT interfaces.

The XRD profiles of the sintered pellets are presented in Fig. 3. Sintering at 980 °C gives minor peaks likely assigned as Li_2ZrO_3 [20] and $La_2Li_{0.5}Co_{0.5}O_4$ [21] compounds, but these peaks are hardly discernible in the profile for 1080 °C, instead minor peaks likely assigned as $LaCoO_3$ compound become visible. Yet the major peaks of LCO and LLZT do not show significant attenuation or lateral shifts, suggesting that phase changes could take place only in specific regions. It is important to note that the detection limit for phase identification by conventional XRD is known to be around 4 vol% [22]. Although being a rough estimation, the volume fractions of the observed interphases IP-I, IP-I′, and IP-II (detailed explanations of which are given later) are 3.5, 1.2, and 0.1 vol%, respectively. Therefore, these interphases are unlikely to be detectable from the XRD profiles. A closer look at the peak shape reveals that the peak widths become somewhat sharper by high-temperature sintering. This change is supposed to be a consequence of thermal relaxation and thereby the release of lattice defects.

Thermodynamic calculations were performed for the LCO-LLZT binary system using two databases: one is the FactPS database supplemented with the ab initio Material Project (AiMP) ver. 4.0 for experimentally unknown compounds, and the other is AiMP ver. 6.3. The results at 1000 °C are shown in Fig. 4(a) and (b), respectively. Fig. 4 (a) shows no reaction between LCO and LLZT occurs. Fig. 4(b) indicates that although LLZT tends to decompose into more thermodynamically stable compounds, no reaction takes place between LCO and them. These results substantiate the low reactivity between LCO and LLZT (or its decomposition products).

3.2. Sintered microstructure

Micro/nanoscale observations are indispensable for evaluating the degree of densification and interfacial contact of the sintered pellets. In

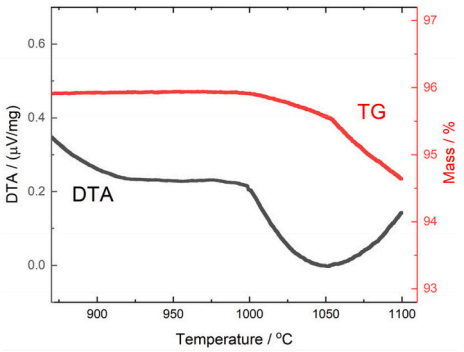

Fig. 1. TG-DTA curves obtained under 95 %O_2–5 %Ar gas flow.

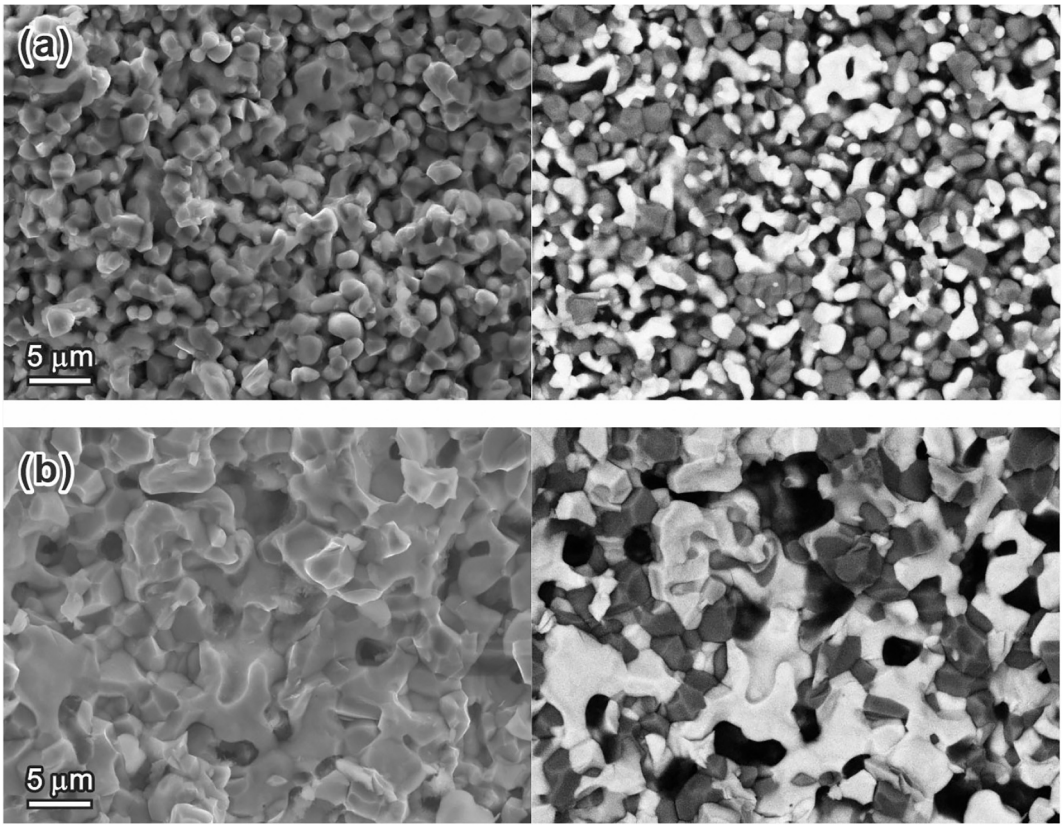

Fig. 2. SEM images of the fracture surfaces of the pellets sintered at (a) 980 and (b) 1080 °C, where the left and right panels correspond to the secondary and backscattered electron images of the same field of view, respectively. The bright and dark areas in the backscattered electron images correspond to the LLZT and LCO phases, respectively.

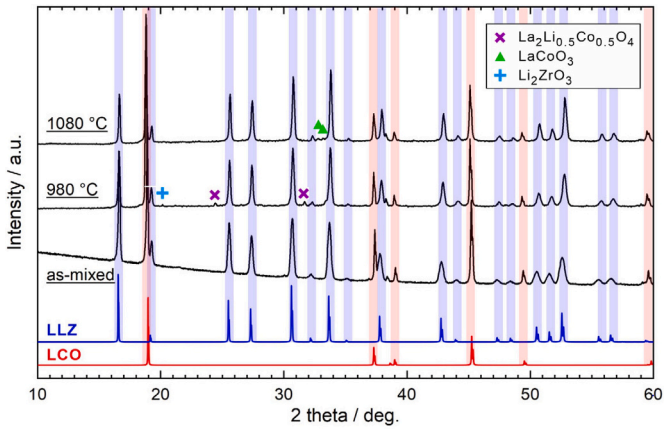

Fig. 3. XRD profiles of the LCO + LLZT powders as mixed and sintered at 980 and 1080 °C along with reference XRD profiles of LCO (red) [18] and LLZ (blue) [19]. (For interpretation of the references to colour in this figure legend, the reader is referred to the web version of this article.)

Figs. 5 and 6, the microstructures and corresponding elemental maps of the pellets sintered at 980 and 1080 °C are shown, respectively. The most salient feature is that the morphology differs dramatically between these microstructures. The microstructure in Fig. 5(a) is filled with micro-meter scale LCO and LLZT particles with high porosity, which reminds us that the sintering reaction does not proceed actively at 980 °C. A small amount of impurities is visible in Fig. 5(b): as a result of electron diffractions taken from these areas, red- and blue-colored particles are identified as Li_2ZrO_3 and $La_2Li_{0.5}Co_{0.5}O_4$, respectively (see Supplemental Fig. 1), which are in full agreement with the impurities instructed by XRD (Fig. 3).

The densification progresses dramatically at 1080 °C, accompanied by morphological change of both the LCO and LLZT particles. This change is likely a consequence of an endothermal reaction above 1000 °C detected in the DTA curve (see Fig. 1). The highly densified microstructure shown in Fig. 6 seems desirable from the perspective of tailoring the microstructure for ASSLIBs. Yet, the LCO/LLZT interfacial nanostructure is responsible for the ionic conduction between LCO and LLZT phases. In what follows, the nano- or even atomic structures of the LCO/LLZT interface are discussed in detail.

3.3. LCO/LLZT interfacial microstructure sintered at 980 °C

The dataset of STEM observations and EDS analysis of the LCO/LLZT interface sintered at 980 °C is presented in Fig. 7. The EDS line profiles in Figs. 7(b)–(f) reveal that the mutual diffusion takes place toward the interior of the LLZT phase over a width of approximately 20 nm. The constituent elements of La, Zr, and Ta gradually deplete, and instead, Co intervenes from the contacting LCO phase. The crystal structures of LCO and LLZT are robust up to the interface and thus no interfacial phase is confirmed. No specific relationship is found between the crystal orientations of adjacent LCO and LLZT grains from the FFT patterns in Fig. 7 (g).

It should be noted that the profiles overlaid on the EDS maps represent the detected intensities and not the chemical compositions since the Li concentration is not accessible with this technique. According to a study using an inductively coupled plasma optical emission spectroscopy by Din [23], Co contamination into LLZ can lead to the degradation processes even in very small amounts of 0.67 at.% (corresponding to 0.16 per formula unit). From a practical perspective, therefore, the extent of Co contamination deep inside the LLZT is one of

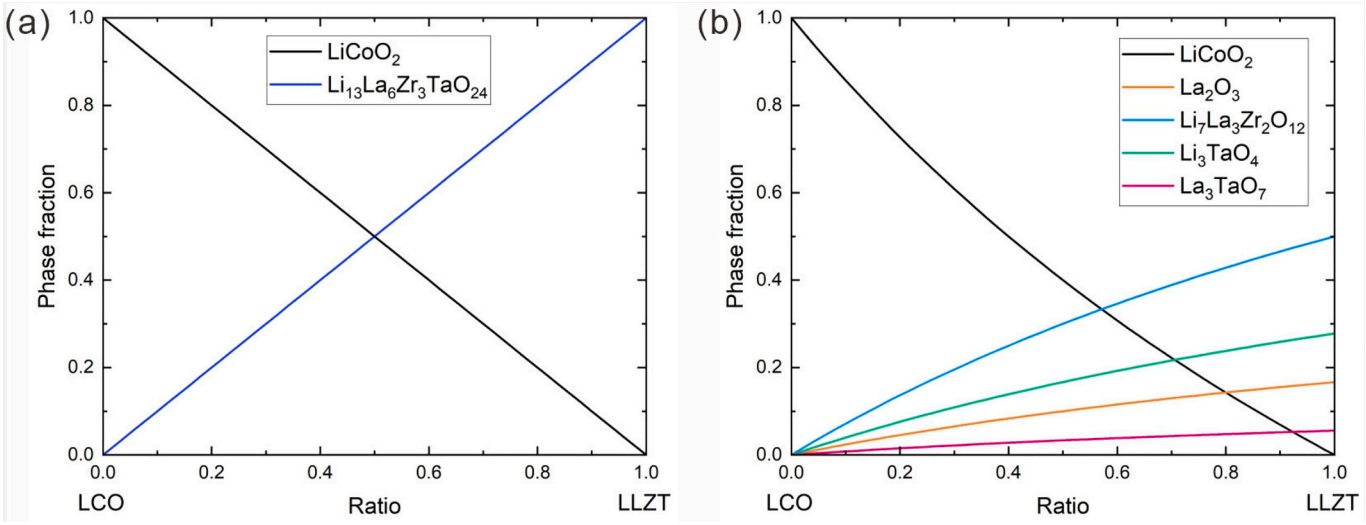

Fig. 4. Thermodynamic stability for the LCO-LLZT system at 1000 °C derived using the databases of (a) the FactPS supplemented with AiMP ver. 4.0 and (b) AiMP ver. 6.3.

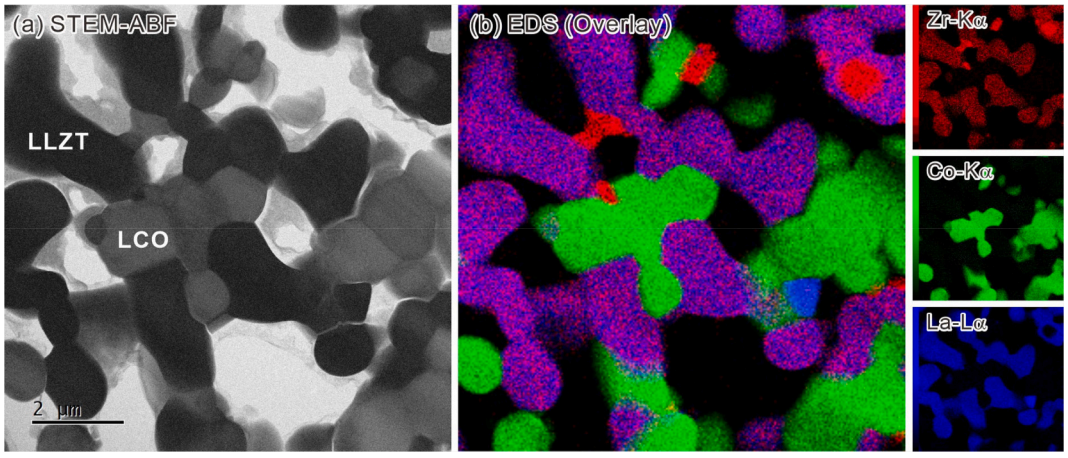

Fig. 5. Microstructure sintered at 980 °C. (a) STEM-ABF image and (b) corresponding EDS map colour-coded with Zr-Kα (red), Co-Kα (green), and La-Lα (blue) intensities. (For interpretation of the references to colour in this figure legend, the reader is referred to the web version of this article.)

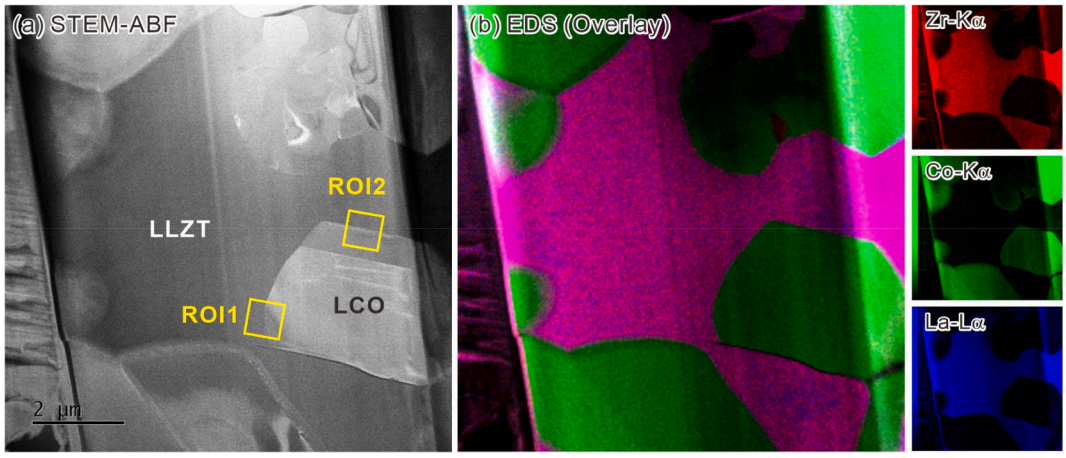

Fig. 6. Microstructure sintered at 1080 °C. (a) STEM-ABF image and (b) corresponding EDS map colour-coded with Zr-Kα (red), Co-Kα (green), and La-Lα (blue) intensities. (For interpretation of the references to colour in this figure legend, the reader is referred to the web version of this article.)

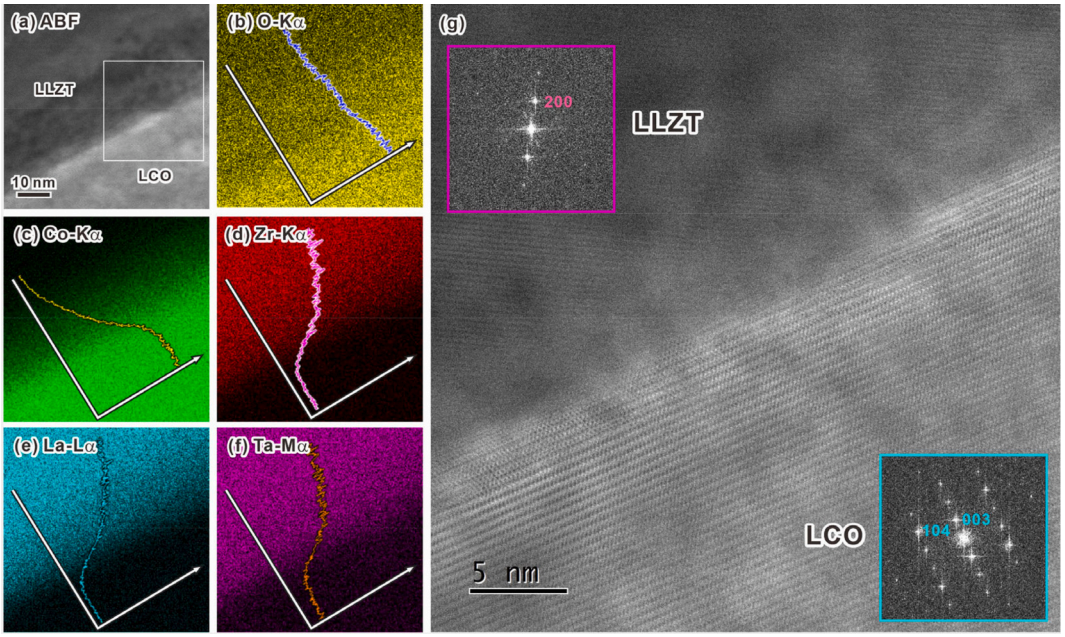

Fig. 7. Microstructure in vicinity of the LCO/LLZT interface sintered at 980 °C. (a) STEM-ABF image and corresponding EDS map for (b) O-Kα, (c) Co-Kα, (d) Zr-Kα, (e) La-Lα, and (f) Ta-Mα. (g) Magnified STEM-ABF image of the rectangle area in (a) and FFT patterns generated from LCO and LLZT regions. In (b)-(f), the integrated intensity profiles are overlaid.

the important concerns. However, due to the lack of Li distribution information and limited precision (approximately 1 at.%), the EDS measurements employed in this study are not capable of measuring quantitative Co distribution.

3.4. LCO/LLZT interfacial microstructure sintered at 1080 °C (ROI-1)

As far as we can find, there are two types of the LCO/LLZT interface in terms of the constituting crystallographic structures, thickness, and chemical composition: one is a narrow and well-tailored interface with moderate chemical gradation, and the other is a broad and multi-layered interface with irrational chemical distribution. These interfaces are respectively observed in the regions of interest, "ROI-1" and "ROI-2", highlighted in Fig. 6.

A magnified image and corresponding EDS maps of ROI-1 are presented in Fig. 8. The interface is constituted with one interphase, herein referred to as "IP-I". As shown in the overlaid profiles in Fig. 8(b)-(f), the IP-I is capable of significant chemical variation, linearly connecting the compositions of the constituent elements of LCO and LLZT, i.e., O, Co, Zr, La, and Ta.

The detailed crystal structure of IP-I can be inferred from the high-resolution STEM-HAADF image shown in Fig. 9(a). Typical FFT patterns for the LLZT, IP-I, and LCO phases are inserted in Fig. 9(b). The IP-I and LCO phases are in coherent contact and have nearly identical crystallographic symmetry, while any lattice correspondence or crystallographic similarity does not exist between the adjacent IP-I and LLZT phases. The intensity ratio of 003 and 104 spots, i.e., I_{003}/I_{104} in the generated FFT patterns can be a measure to evaluate the degree of ordering of the Li and Co sites in the LCO structure. As shown in Fig. 9 (b), this value changes linearly in the IP-I phase. This value is

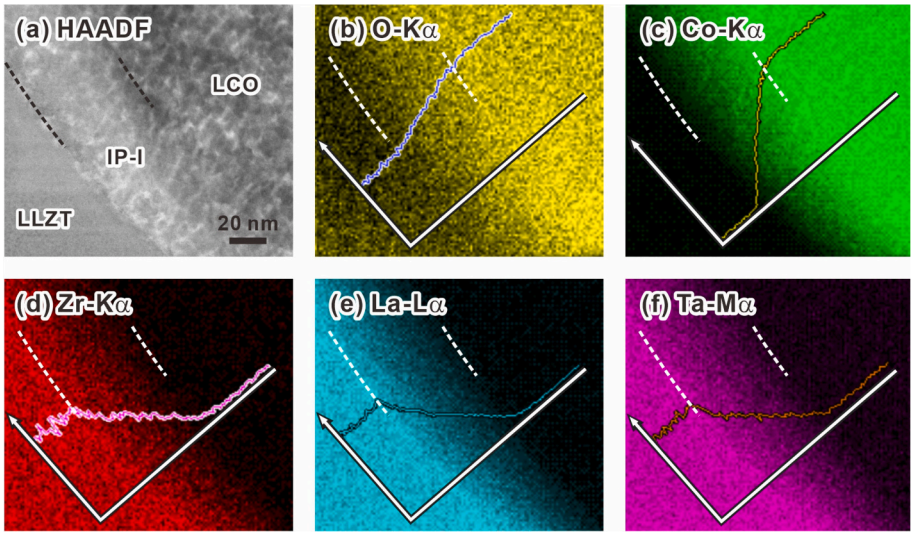

Fig. 8. Microstructure and EDS maps of ROI-1: a thin LCO/LLZT interface sintered at 1080 °C. (a) STEM-HAADF image and corresponding EDS map for (b) O-Kα, (c) Co-Kα, (d) Zr-Kα, (e) La-Lα, and (f) Ta-Mα. In (b)-(f), the integrated intensity profiles are overlaid.

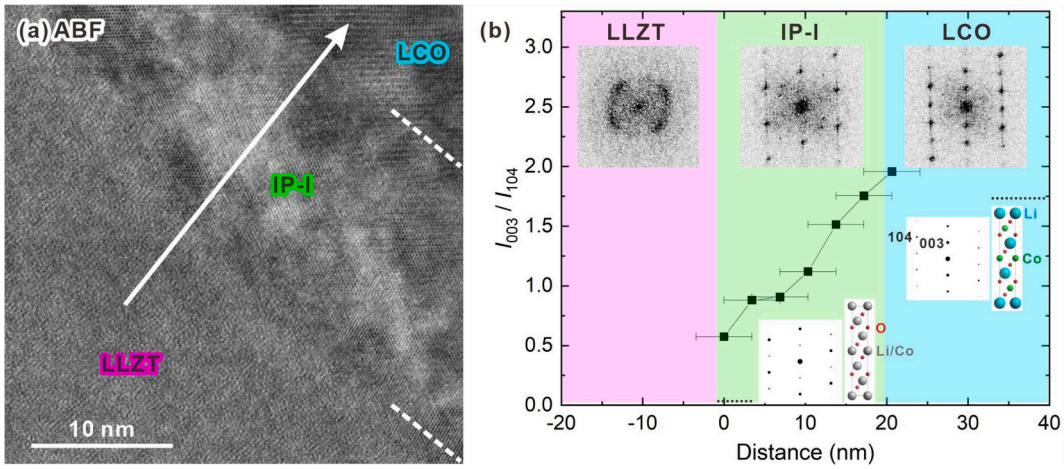

Fig. 9. (a) STEM-ABF image in vicinity of IP-I. (b) A profile of intensity ratio I_{003}/I_{104} along the arrow in (a), where I_{003} and I_{104} indicate the integrated intensities of 003 and 104 spots in the FFT patterns. Indices 003 and 104 are assigned with reference to the LCO crystal structure. FFT patterns are generated for rectangle areas with sides of ~7 nm in (a). The simulated I_{003}/I_{104} values for the fully ordered and disordered LCO structures are leveled by dot lines together with their simulated electron diffractions and crystal structures.

comparable to that of a perfectly ordered LCO structure near the LCO/IP-I boundary while drops to that of a significantly disordered state as the LLZT/IP-I boundary is approached. This lowering in cation ordering is supposed to be due to the intermixing of the Li and Co layers: at the front of the LLZT/IP-I boundary, the cation sites are randomly occupied by Co and Li (see the reference structure in Fig. 9(b)). From what we have observed, the thickness of IP-I is relatively thin, ranging from 2 to 20 nm.

The electronic structures, especially the valence states, of the constituents of IP-I are of particular importance in inferring ionic conductivity across the interface. The EELS spectra are acquired for the ROI-1 and the core-loss spectra integrated over the rectangles in Fig. 10(a) are presented in Fig. 10(b). The EELS spectrums of LCO and IP-I are similar, as inferred from the crystallographic similarity. As the LLZT/IP-I boundary approaches, the Co-L_3 and -L_2 peak intensities weaken, supplanted by an increase in the La-M_5 and -M_4 peaks. This trend is qualitatively consistent with the EDS result shown in Fig. 8. The valence number of Co can be evaluated from the intensity ratio of the Co-L_3 and -L_2 peaks [24]. As shown in Fig. 10(c), this ratio in IP-I changes little (or slightly upshifts) compared to the ratio in LCO, and is placed between the ratio of Co_3O_4 and $CoSi_2$. This means that the valence number of IP-I is estimated to be approximately +3, the same as LCO (or slightly smaller). Substituted elements such as Zr and Ta are supposed to adopt valence numbers greater than +3 to compensate for electroneutrality.

The intensity ratio of the O—K pre-peak I_{pre} and main peak I_{main} is also informative in inferring the Li concentration and electronic structure in the conduction band around the O ion [25,26]. According to an earlier EELS study by Graetz [26], the O ions are primarily responsible for compensating the charge valance in response to the Li depletion in LCO, rather than modifying the valence number of Co-site ions. The I_{pre}/

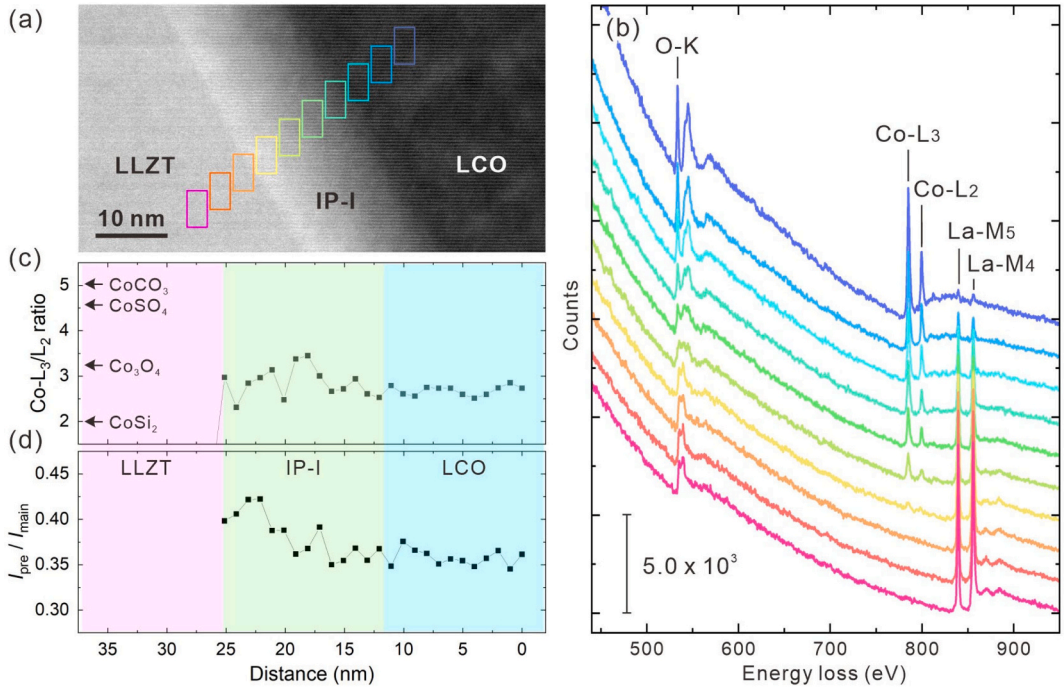

Fig. 10. EELS analysis for ROI-1. (a) STEM-HAADF image in vicinity of IP-I. (b) EELS spectra accumulated for the rectangles in (a). (c) The integrated intensity ratio of the Co-L_3 and -L_2 peaks. (d) The integrated intensity ratio of the O—K pre-peak and main peak.

I_{main} ratio refers to the density of O 2p holes, which could be introduced by the Li extraction. We thus can infer the Li deficiency from the I_{pre}/I_{main} ratio. As shown in Fig. 10(d), the ratio in the IP-I is almost the same as that in the adjacent LCO at the LCO/IP-I interface but gradually increases with distance. This behavior again follows the structural similarity between LCO and IP-I: although the chemical constituent is gradually modified with distance from the LCO/IP-I boundary, the hosting crystal structure is essentially the same. The upshift in I_{pre}/I_{main} while maintaining the Co-L_3/L_2 ratio corroborates that the O atoms are more involved in the charge transfer than the Co atoms in response to Li deficiency. It seems to be a reasonable scheme that the IP-I phase is Li deficient, which results in electron depletion in the O 2p states, making the O—Co bond more covalent.

3.5. LCO/LLZT interfacial microstructure sintered at 1080 °C (ROI-2)

The well-tailored thin interface representatively observed in ROI-1 is characterized as the intervention of a single-phase IP-I (2–20 nm thick). Its structural, chemical, and electronic characters are relatively easy to interpret. On the other hand, there exists a relatively thick LCO/LLZT interface (over 50 nm thick) with multi-phase configurations, represented by ROI-2.

As shown in Fig. 11(a), the interface configuration seen in ROI-2 is somewhat complicated. The thickest layer phase contacting the LCO is labeled as IP-I, which has a coherent lattice matching to the LCO, as confirmed by the FFT pattern shown in Fig. 11(b). With increasing distance from the LCO, the crystallographic morphology changes to modulated nanodomains, blurring the FFT pattern as shown in the atom-resolved image (see second raw from the top of Fig. 11(b)). Above this interlayer phase (labeled as IP-I′), a well-tailored, very thin interfacial phase (labeled as IP-II) emerges in contact with LLZT. Its high-resolution image and FFT pattern (the top raw of Fig. 11(b)) suggest the incoherency with the IP-I′.

To evaluate the crystal structure more intuitively, radial averaged one-dimensional (1D) profiles of the FFT patterns shown in Fig. 11(b) are provided in Fig. 11(c) together with those calculated for some compounds, which are anticipated to emerge in the LCO/LLZT sintering system [20,27–31]. Note that the experimental 1D FFT profiles are generated only for the observed beam incident, thus are deficient in unresolved lattice periodicities. Nevertheless, peak positions of IP-I are placed near those of the disordered LCO. The peaks of IP-I′ is similar to those of the ordered LCO rather than the disordered LCO. The 1D FFT profile of IP-II does not resemble any reference materials shown. The detailed crystal structure of IP-II has not been identified in this study.

Elemental distributions in ROI-2 are shown in Fig. 12. Although not linear, the decremental trend of O and Co toward the LLZT side is consistent with the case of ROI-1. Both the IP-I and IP-I′ phases are assumed to have similar chemical and structural features. On the other hand, Zr, La, and Ta are not diffused into these phases unlike in the IP-I in ROI-1. Chemical gradation in the IP-II is totally different from those of the IP-I and IP-I′. Very steep chemical changes exist inside IP-II, swinging back all the values comparable to the stoichiometry of LLZT. This suggests that the IP-II works as a strong barrier for mutual chemical diffusion.

In the same manner as Fig. 10, spatially resolved EELS spectra, the Co-L_3/L_2 intensity ratio, and the intensity ratio of the O-K pre-edge and main peak for ROI-2 are summarized in Fig. 13. The spectrum of IP-II is almost the same as that of LLZT. Along with the chemical and structural similarities, the IP-II phase is inferred to be a family/derivative compound of LLZT. The essential features of EELS spectra of the IP-I and IP-I′

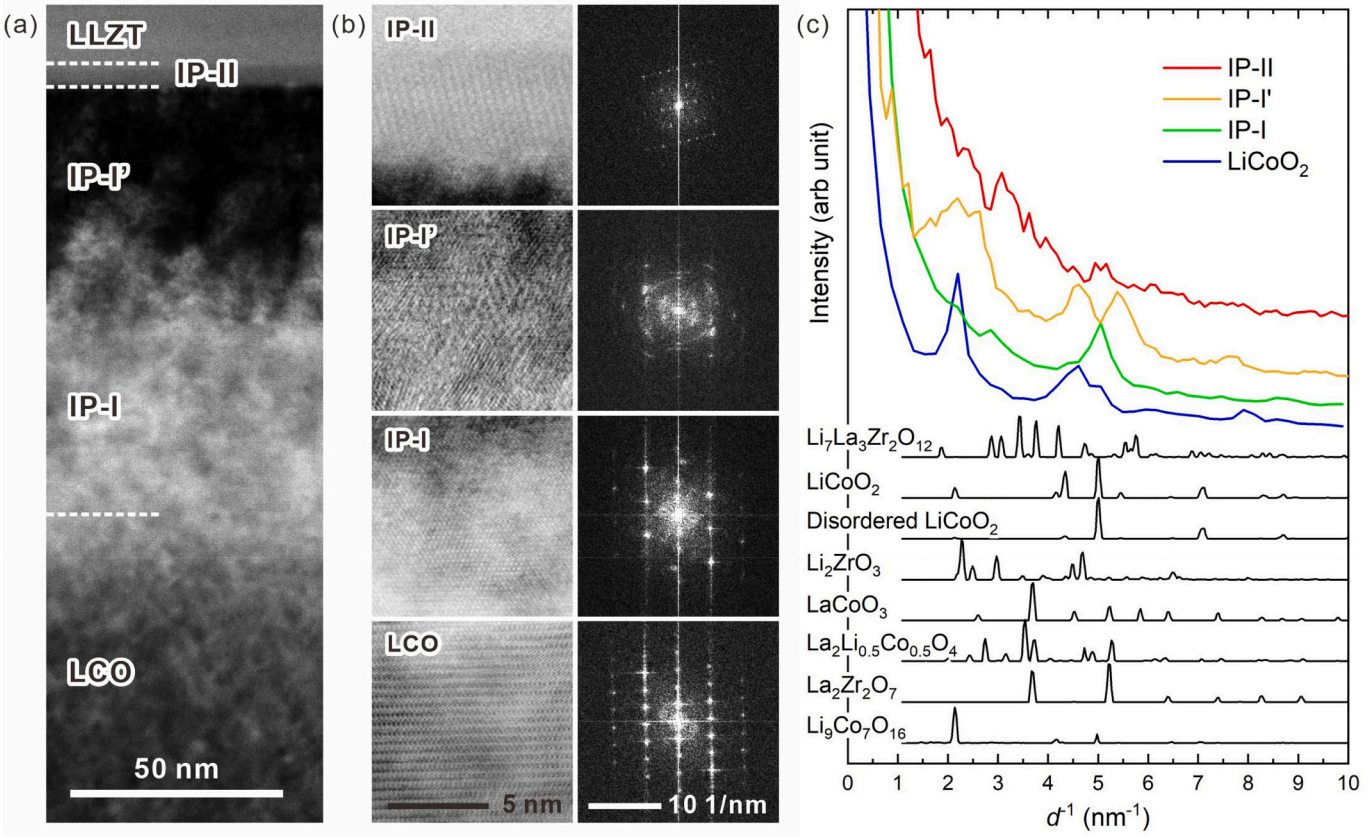

Fig. 11. Microstructure of ROI-2: a thick LCO/LLZT interface sintered at 1080 °C. (a) STEM-HAADF image. (b) High-resolution STEM-HAADF images of the constituting phases and corresponding FFT patterns. (c) Radial averaged one-dimensional intensity profile of the FFT patterns shown in (b) and those of reference materials of cubic $Li_7La_3Zr_2O_{12}$ [19], $LiCoO_2$ [18], disordered $LiCoO_2$, Li_2ZrO_3 [20], $LaCoO_3$ [27], $La_2Li_{0.5}Co_{0.5}O_4$ [3,13,28,29], $La_2Zr_2O_7$ [30], and $Li_9Co_7O_{16}$ [31], which is suggested as a metastable reaction product by the thermodynamic calculations in this study.

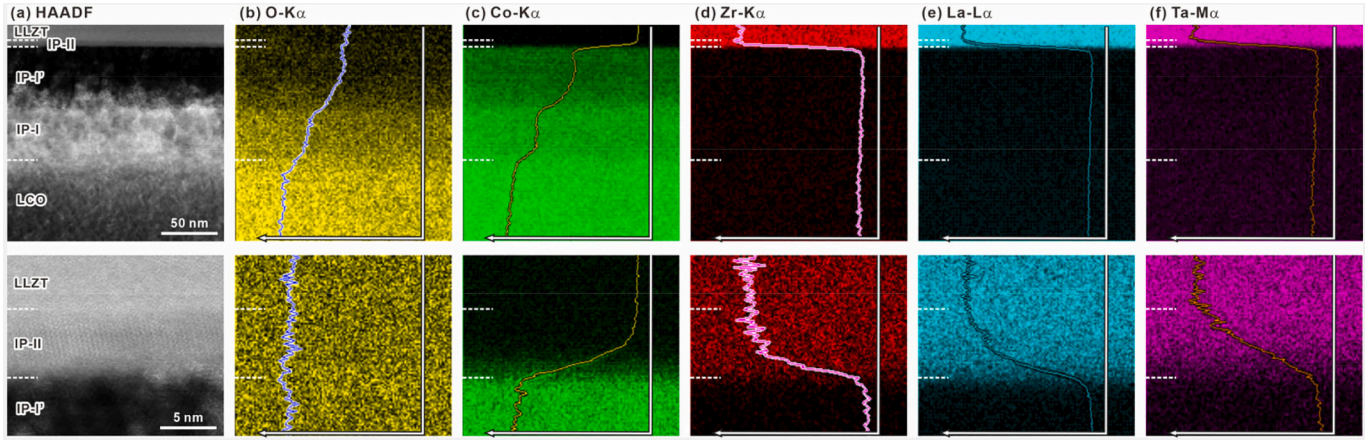

Fig. 12. EDS maps of ROI-2 Upper and lower columns are for an overview of ROI-2 and magnified view in vicinity of IP-II, respectively. (a) STEM-HAADF image and corresponding EDS map for (b) O-Kα, (c) Co-Kα, (d) Zr-Kα, (e) La-Lα, and (f) Ta-Mα. In (b)-(f), the integrated intensity profiles are overlaid.

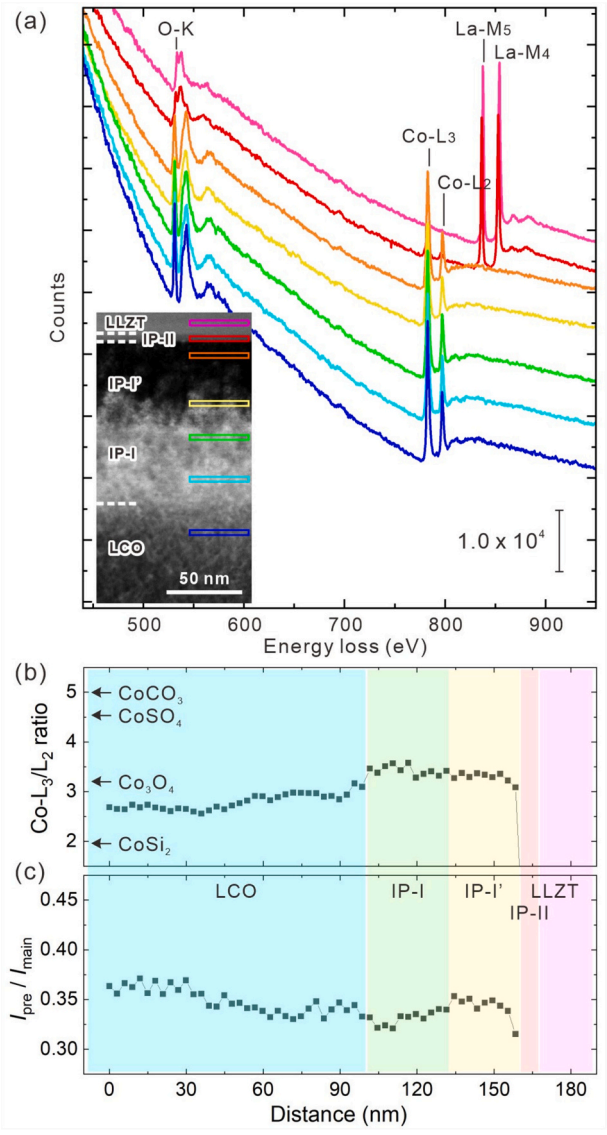

Fig. 13. EELS analysis for ROI-2. (a) EELS spectra accumulated for the rectangles in the inserted STEM-ABF image. (b) The integrated intensity ratio of Co-L_3 and -L_2 peaks. (c) The integrated intensity ratio of the O—K pre-peak and main peak.

phases are the same as that of the IP-I phase seen in ROI-1, but a closer look at the Co-L_3/L_2 ratio and I_{pre}/I_{main} highlights the subtle differences in the valence state. The slight increase in the Co-L_3/L_2 ratio in the IP-I and IP-I′ phases indicates that the valence number of the Co atoms could somewhat downshift from +3. Meanwhile, I_{pre}/I_{main} changes little across the LCO, IP-I, and IP-I′ phases, suggesting that the IP-I and IP-I′ phases are not deficient in Li.

4. Discussion

As far as we can find in the pellet sintered at 1080 °C, the LCO/LLZT interfaces are infiltrated with two types of interfacial products: the LCO-derivative IP-I (and IP-I′) and the well-ordered compound IP-II. As well as the differences in their structural, chemical, and electronic characters, the difference in thickness is worth mentioning. The IP-II phase forms in a very thin (only a few nanometers) layer with well-tailored, well-structured morphology in full contact with the LLZT, suggesting that the IP-II phase is chemically less reactive. The IP-I and IP-I′ phases, in contrast, form in a wide range of thickness from a few to hundreds nanometers, and show significant variations in chemical composition and cation disordering. These features may be delivered from the chemical reactivity of LCO and thus play a dominant role in densification.

A detailed look at the vicinity of the IP-I/IP-I′ boundary is presented in Fig. 14. As shown in the inset of the HAADF-STEM image (Fig. 14(a)), the *c*-plane fringe of the LCO structure terminates at the IP-I/IP-I′ interface. This discrete change is highlighted through the geometrical phase map using the 006/00$\bar{6}$ periodicity of LCO, as shown in Fig. 14(c). The maze-like pattern in the IP-I′ represents the reconstruction failure due to the discernible 006/00$\bar{6}$ periodicity, wherein the randomly oriented crystals form. The clear, well-aligned IP-I/IP-I′ interface indicates that the intermediate state between these phases is mostly likely absent. In addition, the brighter contrast of the IP-I′ region in the HAADF-ABF image (Fig. 14(b)) suggests that this region involves a significant degree of strain. From these microstructural characters, it is suggested as a reasonable scenario that the IP-I′ phase forms through a severe morphological change such as melting and sublimation. Indeed, the reactive temperature of LCO has been reported to be about 900 °C [14], which is lower than that of LLZT of 980 °C [16,17].

The LCO structure comprises alternative Co- and Li-layers stacking along ⟨111⟩ direction of the rock-salt lattice. The crystallographic disordering of this structure is accompanied by the increase in the crystallographic symmetry toward cubic NaCl or spinel-related type [26]. In view of structural coherency and morphology, the IP-I could be formed with the help of bulk diffusion at the LCO/LLZT interface with keeping

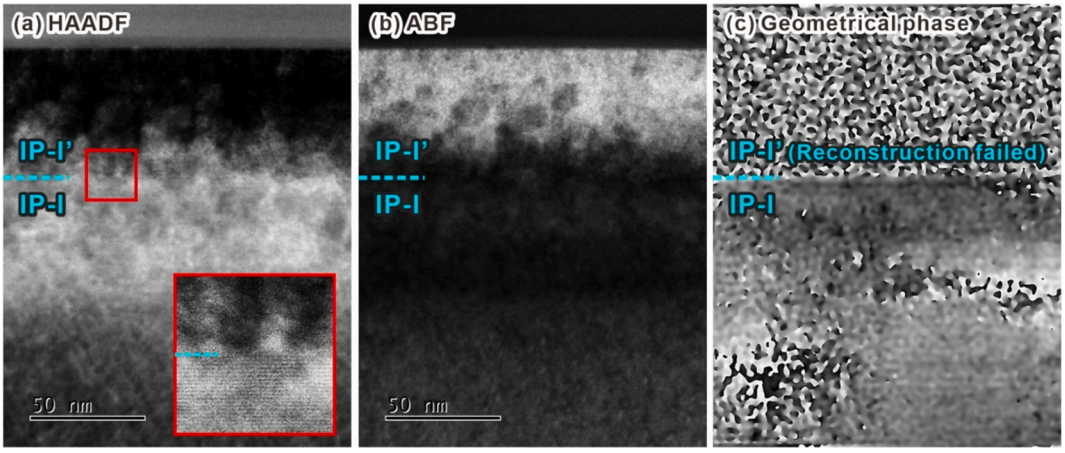

Fig. 14. Enclosed (a) STEM-HAADF and (b) STEM-ABF images of a thick LCO/LLZT interface sintered at 1080 °C. (c) Geometrical phase map reconstructed from (a) using 006/00$\bar{6}$ periodicity of LCO.

the structural coherency to the contacting LCO. Meanwhile, the IP-I′ could be further formed via the volumetric and surface diffusions or even partial melting of LCO, resulting in the formation of less-crystalized nanodomains. Guess that the highly mobile IP-I′ phase can preferentially infiltrate into voids, this phase would play a major role in the densification upon sintering at 1080 °C.

It is important to address that the disordered cubic-like LCO is reported to be easily formed at 400 °C [32–35]. Although puzzling intuitively, the fact that the preferentially formed IP-I has a disordered structure and the IP-I′ phase formed in a radical diffusion environment has an ordered structure does not contradict the temperature-structure relation reported in previous studies. The disordered LCO is known to exhibit poor charge/discharge characteristics compared to the ordered LCO [35]. Although dramatic densification can be achieved by 1080 °C sintering, the formation of multi-layered and relatively thick interfaces with chemical gradation could be destructive in achieving undisturbed ionic conductivity across the interfaces.

5. Summary

In this study, the microstructural, chemical, and electronic characters of LCO/LLZT pellets sintered at 980 and 1080 °C have been investigated, with a particular focus on the LLZT/LCO interfaces, using an integrated suite of scanning transmission electron microscopy and spectroscopic techniques. Sintering at 980 °C is insufficient to promote densification of the pellet. No interfacial products are confirmed, but instead a chemical gradient is recognized over a width of ~20 nm near the LLZT/LCO interface. Sintering at 1080 °C is quite effective in densification of the pellet. However, two kinds of interlayer products are formed: one is the IP-I and IP-I′ phases with a disordered LCO structure, which form in contact with LCO and is capable of significant chemical gradient inside, and the other is the IP-II phase, of which crystal structure cannot be determined, forming in contact with LLZT. It is assumed that the IP-I′ phase plays a key role in the densification of the pellet. Its low crystallinity reflects the potentially high surface/bulk diffusivity. However, the conformed interfaces suffer from a significant chemical gradient, suggesting poor ionic conductivity across the interfaces.

CRediT authorship contribution statement

K. Niitsu: Writing – original draft, Investigation, Formal analysis, Data curation, Conceptualization. **F. Ichihara:** Writing – review & editing, Investigation, Formal analysis, Data curation. **S. Miyoshi:** Writing – review & editing, Supervision, Investigation, Formal analysis, Data curation. **M. Ode:** Writing – review & editing, Investigation, Formal analysis, Data curation. **K. Mitsuishi:** Writing – review & editing, Supervision, Project administration, Formal analysis, Data curation, Conceptualization. **T. Masuda:** Writing – review & editing, Supervision, Project administration, Funding acquisition, Data curation, Conceptualization. **K. Takada:** Writing – review & editing, Validation, Supervision, Project administration, Funding acquisition, Data curation, Conceptualization.

Declaration of competing interest

The authors declare that they have no known competing financial interests or personal relationships that could have appeared to influence the work reported in this paper.

Acknowledgment

The authors acknowledge the financial support provided by the Materials Processing Science project “Materealize” of the Ministry of Education, Culture, Sports, Science and Technology of Japan (MEXT; Grant Number JPMXP0219207397).

Appendix A. Supplementary data

Supplementary data to this article can be found online at https://doi.org/10.1016/j.ssi.2025.116804.

Data availability

Data will be made available on request.

References

[1] K. Takada, Progress and prospective of solid-state lithium battery, Acta Mater. 61 (2013) 759–770.
[2] R. Chen, Q. Li, X. Yu, L. Chen, H. Li, Approaching practically accessible solid-state batteries: stability issues related to solid electrolytes and interfaces, Chem. Rev. 120 (2020) 6820–6877.
[3] K.H. Kim, Y. Iriyama, K. Yamamoto, S. Kumazaki, Characterization of the interface between LiCoO2 and Li7La3Zr2O12 in an all-solid-state rechargeable lithium battery, J. Power Sources 196 (2011) 764–767.
[4] H. Aono, E. Sugimoto, Y. Sadaoka, N. Imanaka, G. Adachi, Ionic conductivity of solid electrolytes based on lithium titanium phosphate, J. Electrochem. Soc. 137 (1990) 1023–1027.
[5] S. Stramare, V. Thangadurai, W. Weppner, Lithium lanthanum titanates: a review, Chem. Mater. 15 (2003) 3974–3990.
[6] R. Murugan, V. Thangadurai, W. Weppner, Fast lithium ion conduction in garnet-type Li7La3Zr2O12, Angew. Chem. Int. Ed. 46 (2007) 7778–7781.
[7] J. Awaka, N. Kijima, H. Hayakawa, J. Akimoto, Synthesis and structure analysis of tetragonal Li7La3Zr2O12 with the garnet-related type structure, J. Solid State Chem. 182 (2009) 2046–2052.

[8] Y. Wang, W. Lai, Phase transition in lithium garnet oxide ionic conductors Li7La3Zr2O12: the role of Ta substitution and H2O/CO2 exposure, J. Power Sources 275 (2015) 612–620.
[9] P. Badami, J.M. Weller, A. Wahab, G. Redhammer, L. Ladenstein, D. Rettenwander, M. Wilkening, C.K. Chan, A.N.M. Kannan, Highly conductive garnet-type electrolytes: access to Li6.5La3Zr1.5Ta0.5O12 prepared by molten salt and solid-state methods, ACS Appl. Mater. Interfaces 12 (2020) 48580–48590.
[10] T. Thompson, J. Wolfenstine, J.L. Allen, M. Johannes, A. Huq, I.N. Davida, J. Sakamoto, Tetragonal vs. cubic phase stability in Al – free Ta doped Li7La3Zr2O12 (LLZO), J. Mater. Chem. A 2 (2014) 13431–13436.
[11] K. Mizushima, P.C. Jones, P.J. Wiseman, J.B. Goodenough, LixCoO2 (0<x<−1): a new cathode material for batteries of high energy density, Mater. Res. Bull. 15 (1980) 783–789.
[12] Y. Lyu, X. Wu, K. Wang, Z. Feng, T. Cheng, Y. Liu, M. Wang, R. Chen, L. Xu, J. Zhou, Y. Lu, B. Guo, An overview on the advances of LiCoO2 cathodes for lithium-ion batteries, Adv. Energy Mater. 11 (2021) 2000982.
[13] T. Kato, T. Hamanaka, K. Yamamoto, T. Hirayama, F. Sagane, M. Motoyama, Y. Iriyama, In-situ Li7La3Zr2O12/LiCoO2 interface modification for advanced all-solid-state battery, J. Power Sources 260 (2014) 292–298.
[14] F. Ichihara, K. Niitsu, Y. Tanaka, Y. Niwa, K. Mitsuishi, S. Miyoshi, T. Ohno, T. Masuda, Structural analysis of the LiCoPO4 electrode/NASICON-type Li1.3Al0.3Ti1.7(PO4)3 solid electrolyte interface, J. Phys. Chem. C 127 (2023) 15043–15050.
[15] E. Antolini, M. Ferretti, Synthesis and thermal stability of LiCoO2, J. Solid State Chem. 117 (1995) 1–7.
[16] Y. Zhang, F. Chen, R. Tu, Q. Shen, L. Zhang, Field assisted sintering of dense Al-substituted cubic phase Li7La3Zr2O12 solid electrolytes, J. Power Sources 268 (2014) 960–964.
[17] X. Yang, D. Kong, Z. Chen, Y. Sun, Y. Liu, Low-temperature fabrication for transparency Mg doping Li7La3Zr2O12 solid state electrolyte, J. Mater. Sci. Mater. Electron. 29 (2018) 1523–1529.
[18] J. Akimoto, Y. Gotoh, Y. Oosawa, Synthesis and structure refinement of LiCoO2 single crystals, J. Solid State Chem. 141 (1998) 298–302.
[19] J. Awaka, A. Takashima, K. Kataoka, N. Kijima, Y. Idemoto, J. Akimoto, Crystal structure of fast lithium-ion-conducting cubic Li7La3Zr2O12, Chem. Lett. 40 (2011) 60–62.
[20] J.L. Hodeau, M. Marezio, A. Santoro, R.S. Roth, Neutron profile refinement of the structures of Li2SnO3 and Li2ZrO3, J. Solid State Chem. 45 (1982) 170–1179.
[21] T. Takami, Y. Ishikawa, M. Yonemura, T. Fukunaga, E. Matsubara, T. Abe, Crystal structure, ionic conductivity and lithium-ion diffusion pathway in a LaLiCoO system, J. Ceram. Soc. Jpn. 128 (2020) 453–456.
[22] P. Liu, F.S. Khokhar, Quantitative analysis of multi-phase steels of ferrite and austenite, Acta Crystallogr. A62 (2006) s209.
[23] M.M.U. Din, L. Ladenstein, J. Ring, D. Knez, S. Smetaczek, M. Kubicek, M. Sadeqi-Moqadam, S. Ganschow, E. Salagre, E.G. Michel, S. Lode, G. Kothleitner, I. Dugulan, J.G. Smith, A. Limbeck, J. Fleig, D.J. Siegel, G.J. Redhammer, D. Rettenwander, A guideline to mitigate interfacial degradation processes in solid-state batteries caused by cross diffusion, Adv. Funct. Mater. 33 (2023) 2303680.
[24] Z.L. Wang, J.S. Yin, Y.D. Jiang, EELS analysis of cation valence states and oxygen vacancies in magnetic oxides, Micron 31 (2000) 571–580.
[25] H. Xu, Y. Wang, Electron energy-loss spectroscopy (EELS) study of oxidation states of Ce and U in pyrochlore and uraninite – natural analogues for Pu- and U-bearing waste forms, J. Nucl. Mater. 265 (1999) 117–123.
[26] J. Graetz, A. Hightower, C.C. Ahn, R. Yazami, P. Rez, B. Fultz, Electronic structure of chemically-delithiated LiCoO2 studied by electron energy-loss spectrometry, J. Phys. Chem. B 106 (2002) 1286–1289.
[27] A. Wold, R. Ward, Perowskite-type oxides of cobalt, chromium and vanadium with some rare earth elements, J. Am. Chem. Soc. 76 (1954) 1029–1030.
[28] M.A. Nowroozi, S. Ivlev, J. Rohrer, O. Clemens, La2CoO4: a new intercalation based cathode material for fluoride ion batteries with improved cycling stability, J. Mater. Chem. A 6 (2018) 4658–4669.
[29] T. Takami, Y. Ishikawa, M. Yonemura, T. Fukunaga, E. Matsubara, T. Abe, Crystal structure, ionic conductivity and lithium-ion diffusion pathway in a LaLiCoO system, Ceram. Soc. Jpn. 128 (2020) 453–456.
[30] T. Hagiwara, K. Nomura, H. Kageyama, Crystal structure analysis of Ln2Zr2O7 (Ln = Eu and La) with a pyrochlore composition by high-temperature powder X-ray diffraction, J. Ceram. Soc. Jpn. 125 (2017) 65–70.
[31] A. Jain, S.P. Ong, G. Hautier, W. Chen, W.D. Richards, S. Dacek, S. Cholia, D. Gunter, D. Skinner, G. Ceder, K.A. Persson, The materials project: a materials genome approach to accelerating materials innovation, APL Mater. 1 (2013) 011002.
[32] R.J. Gummow, M.M. Thackeray, W.I.F. David, S. Hull, Structure and electrochemistry of lithium cobalt oxide synthesised at 400°C, Mater. Res. Bull. 27 (1992) 327–337.
[33] R.J. Gummow, D.C. Liles, M.M. Thackeray, W.I.F. David, A reinvestigation of the structures of lithium-cobalt-oxides with neutron-diffraction data, Mater. Res. Bull. 28 (1993) 1177–1184.
[34] B. Garcia, P. Barboux, F. Ribot, A. Kahn-Harari, L. Mazerolles, N. Baffier, The structure of low temperature crystallized LiCoO2, Solid State Ionics 80 (1995) 111–118.
[35] R. Kanno, Crystal structure and properties of materials for lithium battery, J. Crystallogr. Soc. Jpn. 40 (1998) 262–271 (in Japanese).